nature communications

Article

https://doi.org/10.1038/s41467-024-55239-1

In situ visualization of interfacial processes at nanoscale in non-alkaline Zn-air batteries

Received: 18 May 2024

Accepted: 4 December 2024

Published online: 30 December 2024

Check for updates

Jiao Wang[1,2], Shuang-Yan Lang[1,2], Zhen-Zhen Shen[1,2], Yan-Liang Zhang[3], Gui-Xian Liu[1,2], Yue-Xian Song[4], Rui-Zhi Liu[1,2], Bing Liu[2,5] & Rui Wen[1,2]

Zn-air batteries (ZABs) present high energy density and high safety but suffer from low oxygen reaction reversibility and dendrite growth at Zn electrode in alkaline electrolytes. Non-alkaline electrolytes have been considered recently for improving the interfacial processes in ZABs. However, the dynamic evolution and reaction mechanisms regulated by electrolytes at both the positive and Zn negative electrodes remain elusive. Herein, using in situ atomic force microscopy, we disclose that thin ZnO_2 nanosheets deposit in non-alkaline electrolyte during discharge, followed by the formation of low-modulus products encircled around them. During recharge, the nanosheets are completely decomposed, revealing the favorable reversibility of the O_2/ZnO_2 chemistry. The circular outlines with low-modulus, composed of C = C and $ZnCO_3$, are left which play a key role in promoting the oxygen reduction reaction (ORR) during the subsequent cycles. In addition, in situ optical microscopy shows that Zn can be uniformly dissolved and deposited in non-alkaline electrolyte, with the formation of homogeneous solid electrolyte interphase. Our work provides straightforward evidence and in-depth understanding of the interfacial reactions at both electrode interfaces in non-alkaline electrolyte, which can inspire strategies of interfacial engineering and material design of advanced ZABs.

Rechargeable Zn-air batteries (ZABs) have been considered one of the promising next-generation energy storage systems because of their low cost, environmental-friendliness, and high theoretical energy density[1–5]. A typical ZAB is operated in alkaline electrolytes, undergoing a $4e^-$ reaction pathway. Basically, O_2 will be reduced to hydroxide ions (OH^-) through the oxygen reduction reaction (ORR) during discharge, and OH^- is reversely oxidized to release O_2 via the oxygen evolution reaction (OER) during recharge ($O_2 + 2H_2O + 4e^- \leftrightarrow 4OH^-$, $E^\circ = 0.40$ V vs. SHE)[6–8]. However, the practical application of ZABs is largely limited by the severe interfacial issues, mainly including the sluggish reaction kinetics of the $4e^-$ transfer oxygen reaction at the air positive electrode and the poor cycle stability from Zn electrode deformation in conventional alkaline electrolytes[9–13].

Recently, researchers found that employing non-alkaline electrolytes can achieve a $2e^-$ ORR reaction at the positive electrode and suppress Zn dendrite formation at the Zn negative electrode, which benefits the ORR/OER reaction kinetics and the interfacial stability of the Zn electrode, respectively[14–18]. For example, in a zinc trifluoromethanesulfonate ($Zn(OTf)_2$) non-alkaline electrolyte, a localized H_2O-poor environment can be formed due to the adsorption of OTf^- on the air electrode, enabling the aprotic $2e^-$ ORR[18,19]. As a result, the ZAB can smoothly operate over 1600 h. Sun et al. reported a

[1]Key Laboratory of Molecular Nanostructure and Nanotechnology, Beijing National Laboratory for Molecular Sciences, CAS Research/Education Center for Excellence in Molecular Sciences, Institute of Chemistry, Chinese Academy of Sciences, Beijing, China. [2]University of Chinese Academy of Sciences, Beijing, China. [3]Thermo Fisher Scientific Ltd, Shanghai, China. [4]School of Energy and Power Engineering, North University of China, Taiyuan, China. [5]State Key Laboratory of Polymer Physics and Chemistry, Beijing National Laboratory for Molecular Sciences, Institute of Chemistry, Chinese Academy of Sciences, Beijing, China. e-mail: ruiwen@iccas.ac.cn

non-alkaline ZAB with excellent cycling performance by employing the zinc acetate aqueous solution as the electrolyte. The discharge product, zinc glycolate dihydrate, showed high reversibility, which allowed the ZAB to operate steadily in the air for almost 600 h[20]. In addition, studies focusing on the negative electrode claimed that dendrite-free Zn growth and high utilization efficiency can be achieved in non-alkaline electrolytes[21,22]. Despite the significant advancements in the electrochemical performance of ZABs, the detailed dynamic processes, reaction pathways, and reaction mechanisms of the electrode/electrolyte interfaces at the nanoscale are far from being well understood due to the difficulties in investigating the complex triple-phase interfacial reactions[23,24]. In situ and high-resolution observations of both positive and negative electrode interfaces, and profound insights into the correlations between the interfacial evolution and electrochemical performance during cycling are urgently required, which is essential for further optimizing the ZABs[25,26].

Herein, mechanistic insights into the interfacial reactions, including the dynamic evolution of the chemical and structural properties at both the positive and Zn negative electrodes, were systematically provided in a $Zn(OTf)_2$-based non-alkaline ZAB. Using in situ atomic force microscopy (AFM), we observed the nanoscale, real-time evolution of the discharge products, ZnO_2, and a circular structure around it upon cell operation. During the discharge, ZnO_2 deposits as nanosheets (the thickness of 1-2 nm) on the Pt electrode surface, along with the circular outlines showing lower modulus. During the recharge, the nanosheets start to decompose from the edge and can be fully reacted. While the circular outlines, composed of $ZnCO_3$ and C = C, remain and promote the deposition of ZnO_2 during the 2nd discharge. In addition, dendrite-free deposition and reversible dissolution processes were clearly monitored on the Zn negative electrode by in situ optical microscopy (OM), which, together with the optimized processes at the positive electrode, contributes to the enhancement of the electrochemical performance of the ZAB. Our work provides direct insights into the interfacial evolution and systematically elucidates reaction mechanisms at both positive electrode and negative electrode interfaces in a non-alkaline ZAB, which is essential for gaining a fundamental understanding of the interfacial reactions and promising strategies for advancing high-performance ZABs.

Results

In situ AFM observations of ORR/OER processes in $Zn(OTf)_2$ electrolyte

The $Zn(OTf)_2$-based non-alkaline electrolyte presents a specific capacity of 812.5 mAh g^{-1} (based on Zn metal) and remains stable for 50 cycles in Zn-air coin cells (Supplementary Fig. S1). In contrast, only 19.8 mAh g^{-1} specific capacity and one cycle can be achieved in alkaline electrolytes, in accordance with Sun's work[18]. To understand the underlying mechanisms regulated by electrolytes, in situ AFM was utilized to further investigate the interface evolution. The scanning electron microscopy (SEM) images of the electrode after discharge verify the favorable ORR activity of Pt nanoparticles (Supplementary Fig. S2). Accordingly, in situ AFM experiment was performed on the Pt-modified highly oriented pyrolytic graphite (HOPG) electrode.

Figure 1a shows the 1st-cycle cyclic voltammetry (CV) curve obtained in an in situ electrochemical cell with O_2-saturated non-alkaline electrolyte (Supplementary Fig. S3). The cathodic peak at 0.99 V is related to the reduction of O_2, and the broad anodic peak around 1.86 V corresponds to the reverse oxidation process. Under an Ar environment, no evident redox peak is observed (Supplementary Fig. S4). In situ AFM was performed to investigate the interfacial evolution during ORR and OER processes. Figure 1b displays the pristine surface of the Pt-modified HOPG electrode at an open circuit potential (OCP) of 1.33 V. Upon discharging, a nanosheet initially appears at 1.11 V on the electrode surface (Fig. 1c). The thickness of the single nanosheet can be clearly measured as 1-2 nm as shown in Supplementary Fig. S5 and the inset of Fig. 1c. As the discharge continues, multiple nanosheets stack together, which corresponds to the ORR proceeding on the Pt electrode (Fig. 1d). The thin nanosheets keep growing and propagating along the horizontal direction (Fig. 1e, f), which possess a large contact area with the substrate and may contribute to a reduced Gibbs free energy during the following decomposition reaction[27,28]. No sediments can be found in the experimental conditions under Ar (Supplementary Fig. S6). In addition, there is no obvious change on the Pt electrode in O_2-saturated alkaline electrolyte because the discharge product of $Zn(OH)_2$ is soluble (Supplementary Fig. S7).

Figure 1g–l exhibits the decomposition process of the nanosheets upon recharging. No significant variation can be observed before 1.66 V (Supplementary Fig. S8). When recharged to approximately 1.78 V, evident decomposition of the nanosheets can be detected, as indicated by the yellow arrows in Fig. 1g, h, which corresponds to the anodic peak in the CV curve. On further proceeding with the OER, the discharge products at the bottom of the image are completely decomposed, whereas the edged structure of the nanosheets remains intact (Fig. 1h–j), referred to as "outline". Note that the circular outline (marked by the blue arrows in Fig. 1j) can be clearly observed on the upper edge of the nanosheet, which is not in direct touch with the Pt substrate. This indicates that the formation of the outlines should be related to the intrinsic properties of the electrochemical reduction reaction, rather than the catalytic effect of Pt nanoparticles. The decomposition reaction gradually proceeds from the edge, as marked by the green arrows in Fig. 1j, k. This finding is more evident in another parallel experiment (Supplementary Fig. S9), providing direct evidence of the decomposition pathway of the products. The nanosheets can be completely decomposed as OER continues, revealing the reversible discharging and recharging processes in the non-alkaline ZAB. However, the circular outlines cannot be decomposed after recharge process as shown in Fig. 1l. The detailed evolution processes during discharge/charge processes are shown in Supplementary Video S1. The corresponding in situ OM images of the interfacial evolution at the Pt electrode are presented in Supplementary Fig. S10. Large-scale in situ AFM images in Supplementary Fig. S11 further confirm the favorable reversibility of the nanosheets, the formation of the circular outlines, and the uniform distribution of the discharge products on the Pt electrode.

Characterizations of the nanosheet and the surrounding outline

Ex situ characterizations were conducted to identify the chemical component and underlying properties of both the nanosheet and its surrounding outline. The high-resolution transmission electron microscopy (HRTEM) image of the nanosheet shows lattice fringes with lattice spacing of 2.81 Å and 1.72 Å in non-edge domains, matching well with the (111) and (220) planes of ZnO_2. The image also indicates the presence of a lattice fringe of ZnO (Fig. 2a). In the O 1 s X-ray photoelectron spectroscopy (XPS), the peak at approximately 532.1 eV can be attributed to ZnO_2 (Supplementary Fig. S12)[29]. In addition, X-ray diffractometer (XRD) investigations provide additional insights into the chemical features of the discharge products (Supplementary Fig. S13). The characteristic peaks 31.79°, 36.87°, and 41.42° are visible, corresponding to the lattice planes of (111), (200), and (210) in ZnO_2. The additional peak at 37.3° may originate from the electrolyte decomposition. These results reveal that the discharge products mainly consist of ZnO_2.

As shown in the TEM image in Fig. 2b, an amorphous layer with a thickness of about 5 nm is observed surrounding the edge of the nanosheet. This is in accordance with the outlines found in the in situ AFM experiment. Figure 2c, d provides the topography and the corresponding DMT modulus mapping, respectively, showing the lower modulus of the outlines when compared to the nanosheets (Supplementary Fig. S14), which could indicate a difference in

https://doi.org/10.1038/s41467-024-55239-1

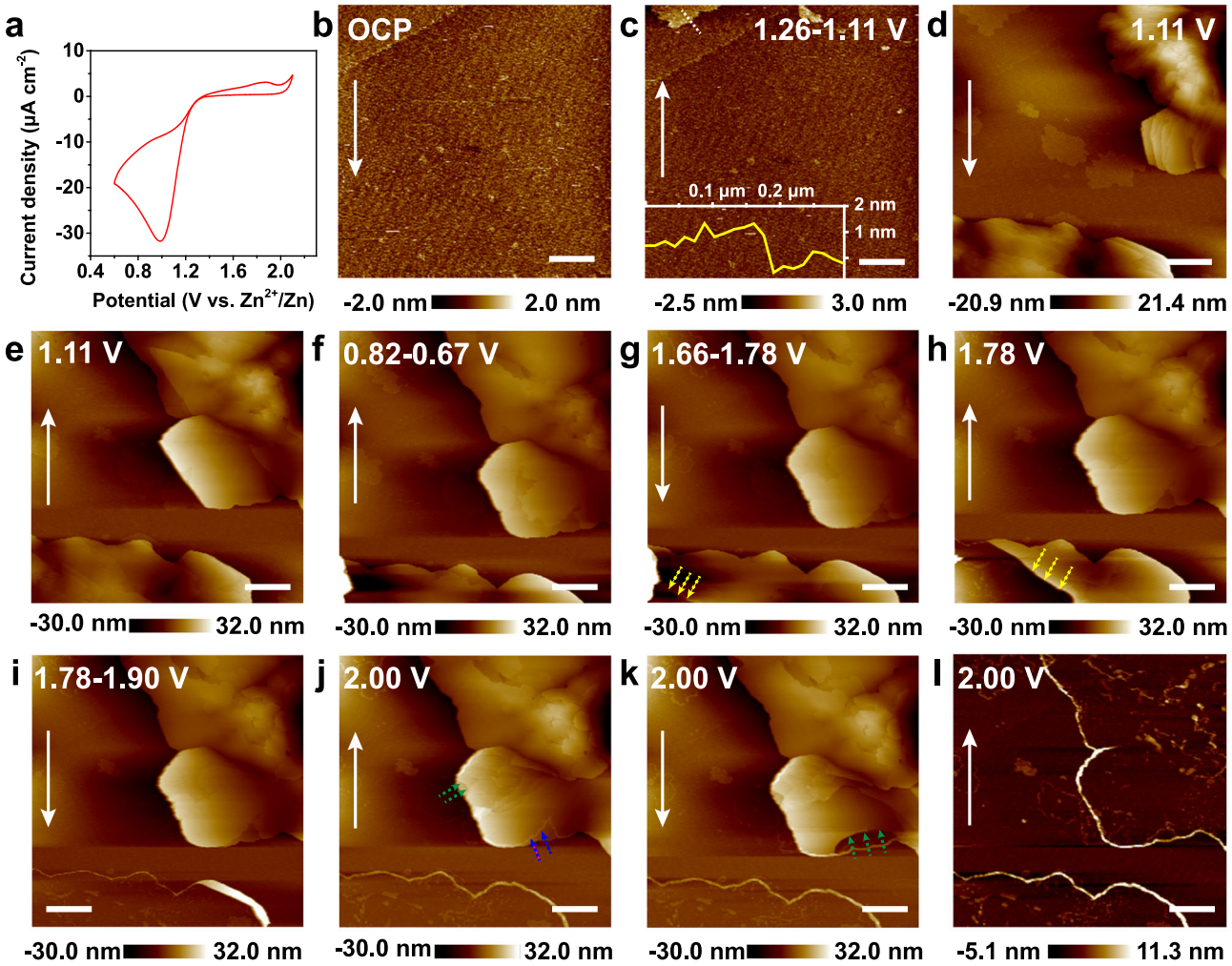

Fig. 1 | In situ AFM monitoring of the ORR/OER processes on the Pt electrode during 1st-cycle. a The 1st-cycle CV curve obtained in the in situ electrochemical cell at a sweep rate of 1 mV s^{-1}. In situ AFM images showing the morphological evolution on the Pt electrode at (**b**) open circuit potential (OCP), upon discharge at (**c**) 1.26-1.11 V, (**d**, **e**) 1.11 V, (**f**) 0.82-0.67 V, and upon recharge at (**g**) 1.66-1.78 V, (**h**) 1.78 V, (**i**) 1.78-1.90 V, (**j**–**l**) 2.00 V. The height profile for the dashed line in (**c**) is shown in the inset of the image. The scale bars are 500 nm. The white arrows indicate the scanning direction.

chemical composition between the nanosheets and outlines. Notably, the varying thicknesses of the stacked nanosheet layers result in differing widths of the outlines left after decomposition. This difference can be seen in Supplementary Fig. S15 (indicated by the black lines), which shows that the thicker layers have outline widths of 21.28 ± 0.38 nm, whereas the thinner layers have outline widths of 5.68 ± 0.22 nm.

TEM, Raman, infrared (IR), and XPS spectra were used to investigate the chemical features of the outlines. The TEM and elemental mapping in Fig. 2e visualize that more C element accumulates on the border while Zn, O, S and F are concentrated on the nanosheet, showing the different chemical compositions of the nanosheets and the outlines. The nanosheet shows a distinct Raman peak at 835 cm^{-1}, attributed to ZnO_2 (Fig. 2f)[30]. While the outline displays a unique peak at 1062 cm^{-1} associated with $ZnCO_3$ (Fig. 2g)[31]. Furthermore, the nanoIR spectra show a characteristic C = C at 960 cm^{-1} for the outline, as depicted in Fig. 2h and Supplementary Fig. S16. The presence of C = C in the outline is further confirmed by the Raman mapping when integrating the peak intensity ratio at 1580 cm^{-1} and 835 cm^{-1}(Supplementary Fig. S17). Besides, the AFM-IR reveals that the absorption peak at 3345 cm^{-1}, corresponding to the O-H stretching vibration mode, is only observed on the outline (Supplementary Fig. S18)[32,33]. XPS (Supplementary Fig. S19) was conducted to further analyze its components (Supplementary Fig. S20 shows the morphology of the sample), which provides the appearance of peaks related to C = C and inorganic $ZnCO_3$ species. The above results indicate that the outlines are rich in C = C and inorganic $ZnCO_3$, which could be formed by the decomposition of the electrolytes.

To better disclose the interfacial mechanism in real systems, the morphology and chemical composition of discharge products in full cells were also investigated. The nanosheets (Supplementary Fig. S21b) with obvious outlines (Supplementary Fig. S21c, d) are observed after discharge, which are assigned to ZnO_2 characterized by XPS and element mapping images (Supplementary Fig. S21e–g). In addition, the outlines remain on the surface of the Pt/C electrode after recharge (Supplementary Fig. S22a, b). These findings are consistent with results obtained from in situ electrochemical cells. Therefore, it is believed that the in situ experiments conducted on electrochemical cells can provide valuable insights into the mechanism and optimization of real battery systems.

Functional role of the outline during the following cycles

The effect of the residual outline during cycling is further disclosed. It is observed that the outlines remain at the Pt electrode after the initial OER process (Fig. 3a). When the potential approaches 1.13 V (Fig. 3b), interestingly, the discharge products of nanosheets tend to generate near the outlines instead of on the bare Pt electrode, which indicates that the residual outlines can improve the ORR activity to a certain extent. In addition, the discharge products form and remain constant

https://doi.org/10.1038/s41467-024-55239-1

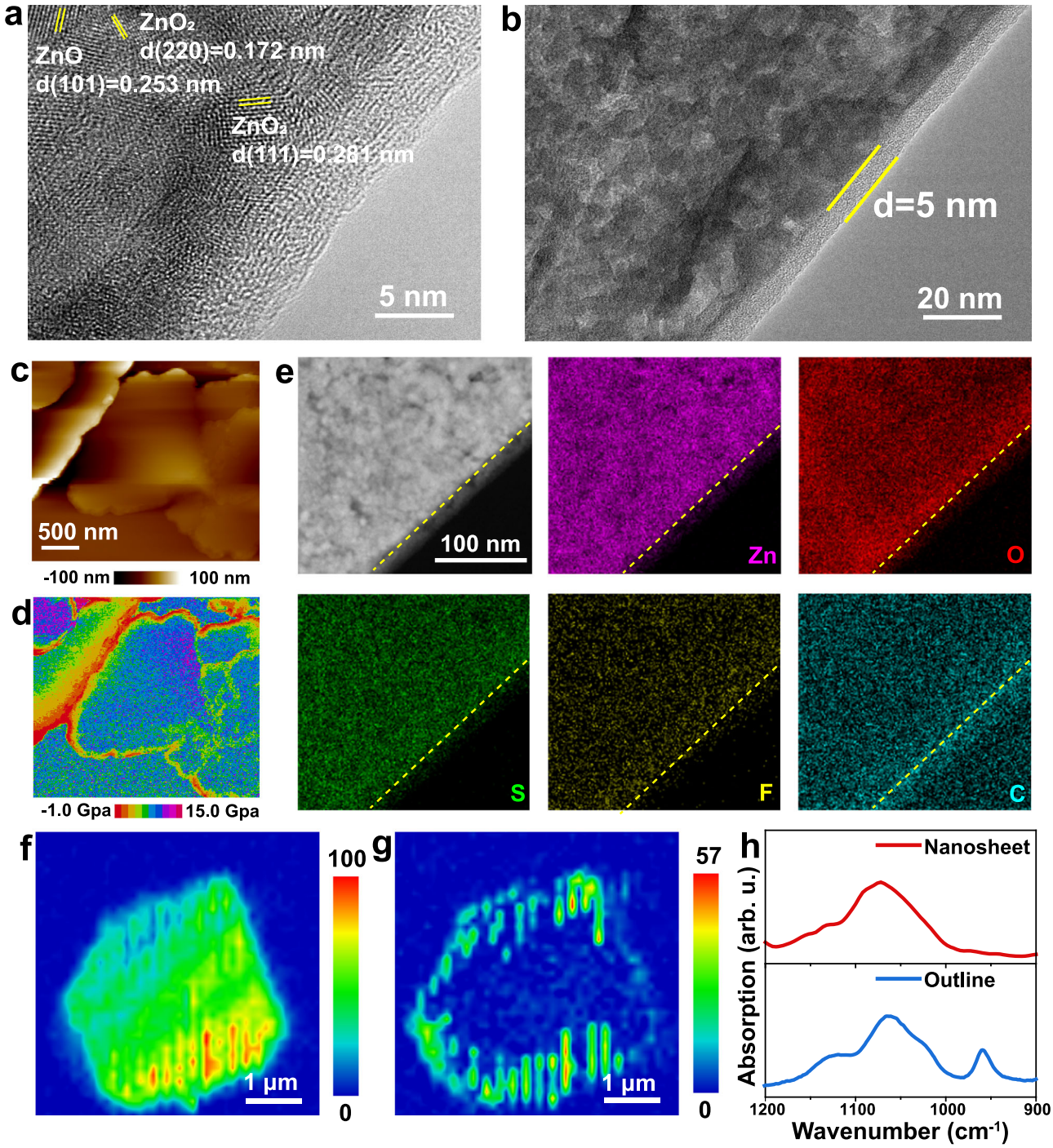

Fig. 2 | Ex situ characterizations of the nanosheet and the surrounding outline. **a**, **b** TEM images of the nanosheet. **c** AFM image and (**d**) corresponding DMT modulus mapping of the deposited products on the Pt electrode after discharge. **e** TEM micrograph with elemental mapping images of the nanosheet. **f**, **g** Raman mappings of the deposited products at 835 cm^{-1} and 1062 cm^{-1}, respectively. **h** IR spectra of the nanosheet and the outline.

within 5 min, but it takes 15 min during the 1st-cycle, suggesting an enhancement in the kinetics process. Thus, we believe that the outlines serve as active sites on the Pt substrate for the subsequent ORR in ZABs. The discharge products are formed on an incline relative to the substrate under the effect of the outlines, which is evidently observed at a larger scale (Fig. 3c, d) and a positive electrode within Zn-air coin cells (Supplementary Fig. S22c, d). In contrast, the nanosheets horizontally grow along the electrode surface during the 1st-cycle since there are no distinct catalytic sites at the bare Pt surface. The schematic illustrations in Supplementary Fig. S23 clearly illustrate the differences in growth patterns. In addition, it noted that the presence of surface defects may serve as sites for preferential crystal growth. To investigate the impact of the surface defect on the discharge process, the Pt-modified HOPG with edges was used as a working electrode to analyze the interface evolution (Supplementary Fig. S24a_1 and b_1). As shown in Supplementary Fig. S24a_{1-4} and b_{1-4}, the nanosheets do not grow along the HOPG edges but instead grow parallel to the electrode surface, similar to the growth mode during 1st-cycle. Therefore, it is believed that the surface defect brought by the outline is not, at least not the primary cause, of guiding product deposition.

During the recharge process, the products begin to decompose at 1.78 V, as marked by yellow arrows in Fig. 3e. In addition, some

https://doi.org/10.1038/s41467-024-55239-1

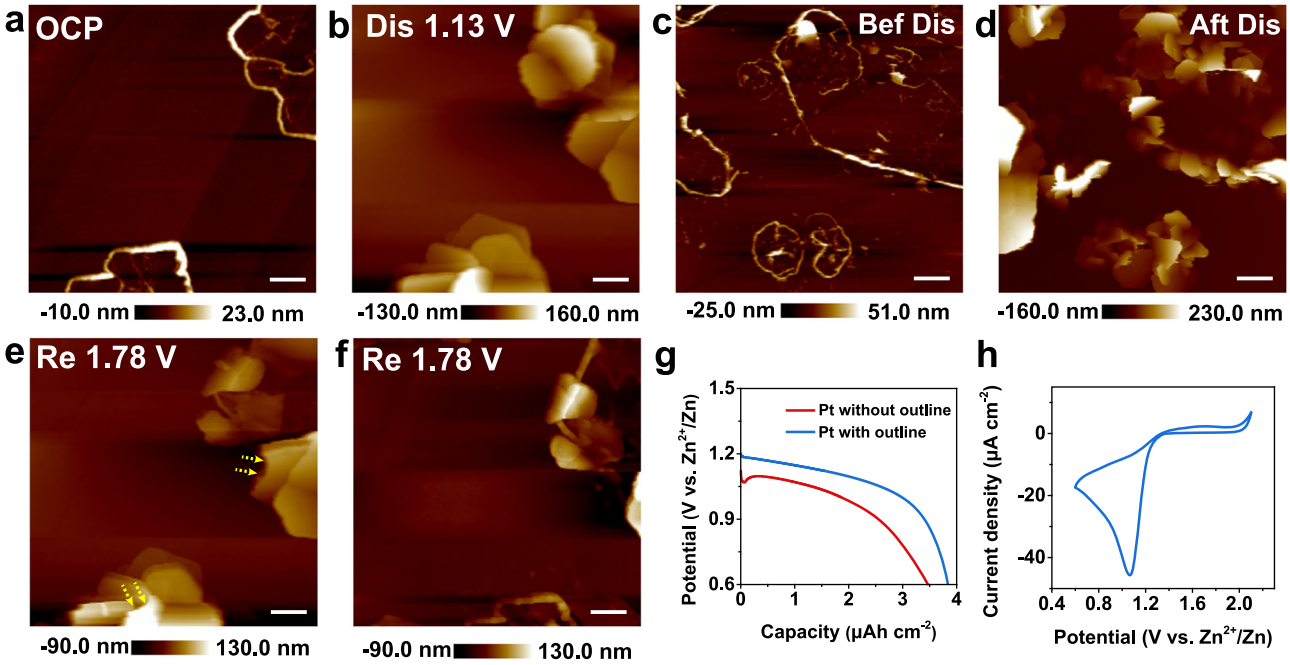

Fig. 3 | In situ AFM images showing the 2nd-cycle morphological evolution on the Pt electrode. In situ AFM images (**a**) at OCP (1.33 V) and (**b**) upon discharge at 1.13 V. AFM images with a larger scale at the end of (**c**) 1st recharge and (**d**) 2nd discharge. **e**, **f** In situ AFM images upon recharge at 1.78 V. The scale bars are 500 nm in (**a**, **b**, **e**, **f**) and 1 μm in (**c**, **d**). **g** Discharge profiles of in situ electrochemical cells with/without the outline at a current density of 40 μA cm^{-2}. **h** The CV curve obtained in the in situ electrochemical cell with the outline-decorated Pt electrode at a sweep rate of 1 mV s^{-1}.

products are desorbed suddenly from the electrode, as indicated in Supplementary Fig. S25, which may be attributed to the detachment of the vertically distributed nanosheets. There is no evident observation of new outlines during the 2nd-cycle, which can be partly due to the growth mode of the nanosheet (Fig. 3f). In addition, the outline remains intact without obvious decomposition during the subsequent cycle with O_2-free electrolyte, indicating excellent stability (Supplementary Fig. S26).

To further investigate the effect of the outline, we use the Pt electrode with outline as working electrode, new Zn strips as counter and reference electrodes, and 1 M $Zn(OTf)_2$ saturated with O_2 for 2 h as electrolyte to test the discharge capacity and CV curves. The discharge capacity increases from 3.46 μAh cm^{-2} to 3.84 μAh cm^{-2} (Fig. 3g), and the cathodic peak at 1.07 V is higher than that in the 1st-cycle (Fig. 3h), indicating improved kinetics in the presence of the outline. The improved performance with the presence of the outline is also evident in Zn-air coin cells, further illustrating its functional effect (Supplementary Fig. S27).

In situ monitoring the interfacial processes at Zn electrode

To achieve a comprehensive understanding of the interfacial processes in ZABs, in situ OM was employed to investigate and compare the Zn electrode/electrolyte interfaces in alkaline (6 M KOH + 0.2 M $Zn(CH_3COO)_2$) and non-alkaline (1 M $Zn(OTf)_2$) electrolytes. To enhance the focus resolving capability, a series of images along the *Z*-axis were taken, which in turn were used to obtain the final height images. The schematic illustration of the homemade in situ electrochemical OM cell is presented in Fig. 4a, in which the polished Zn foils are used as the working and counter/reference electrodes, respectively. The corresponding CV curves of the Zn-Zn cells in the two different electrolytes are displayed in Supplementary Fig. S28. Figure 4b depicts the continuous dynamic evolution processes in the alkaline electrolyte. Several bubbles (indicated by arrows in Fig. $4b_1$) are observed on the Zn surface at OCP. As time increases at OCP, the bubbles become larger, with more fresh ones appearing, and the Zn surface with a metallic luster is darkened (Fig. $4b_2$ and Supplementary Fig. S29), indicating the rapid corrosion of the Zn electrode at OCP. which can be also observed by SEM in detail (Supplementary Fig. S30). During the dissolution process, uneven pits are found on the electrode surface, as shown in the inset of Fig. $4b_3$. This can induce the heterogeneous Zn nucleation during the subsequent deposition process and the dendritic Zn growth as shown in Fig. $4b_4$ and $4b_5$. During the 2nd dissolution process, the deposited Zn dendrites show no evident changes (Fig. $4b_6$ and Supplementary Fig. S31), which indicates that they become "dead" and have poor reversibility. Such uneven deposition and irreversible processes can lead to the accumulation of the Zn dendrite and the shape change of the electrode upon long-life cycles, which hinder the stability of the Zn electrode interface.

The interfacial process of the Zn electrode in the non-alkaline electrolyte was investigated as displayed in Fig. 4c. There is no evident change on the Zn electrode within 0.5 h at OCP (Fig. $4c_1$ and Supplementary Fig. S32), which is different from the corrosion occurring in alkaline electrolyte. When discharged to 0.2 V, the Zn surface becomes darkened homogeneously, indicating a uniform dissolution process (Fig. $4c_2$). During the deposition process, the Zn uniformly forms on the electrode surface, which can be due to the smooth surface after the 1st dissolution process (Fig. $4c_3$). The reversibility of the deposited Zn is disclosed by the 2nd discharge process, as shown in Fig. $4c_4$–c_6. From the height transition of the Zn electrode in Fig. $4c_7$–c_9, it can be found that the heights of the Zn electrode decrease uniformly, further illustrating the homogeneous Zn dissolution process and excellent reversibility. More details of the interfacial evolution on the Zn electrode are shown in Supplementary Video S2 (alkaline electrolyte) and Supplementary Video S3 (non-alkaline electrolyte), respectively.

Furthermore, the morphologies of the Zn electrode after discharge and recharge processes were explored by SEM. As shown in Fig. 4d, e, significantly larger pits are observed on the Zn surface after dissolution in the alkaline electrolyte (Fig. 4d) compared to those formed in the non-alkaline electrolyte (Fig. 4e). After the subsequent deposition process, blocky Zn crystal grain and nanoparticle ZnO, as marked by the white arrows, present on the Zn electrode surface in the alkaline electrolyte (Fig. 4f and Supplementary Figs. S33, 34), which can deteriorate the electrode surface and puncture the battery

https://doi.org/10.1038/s41467-024-55239-1

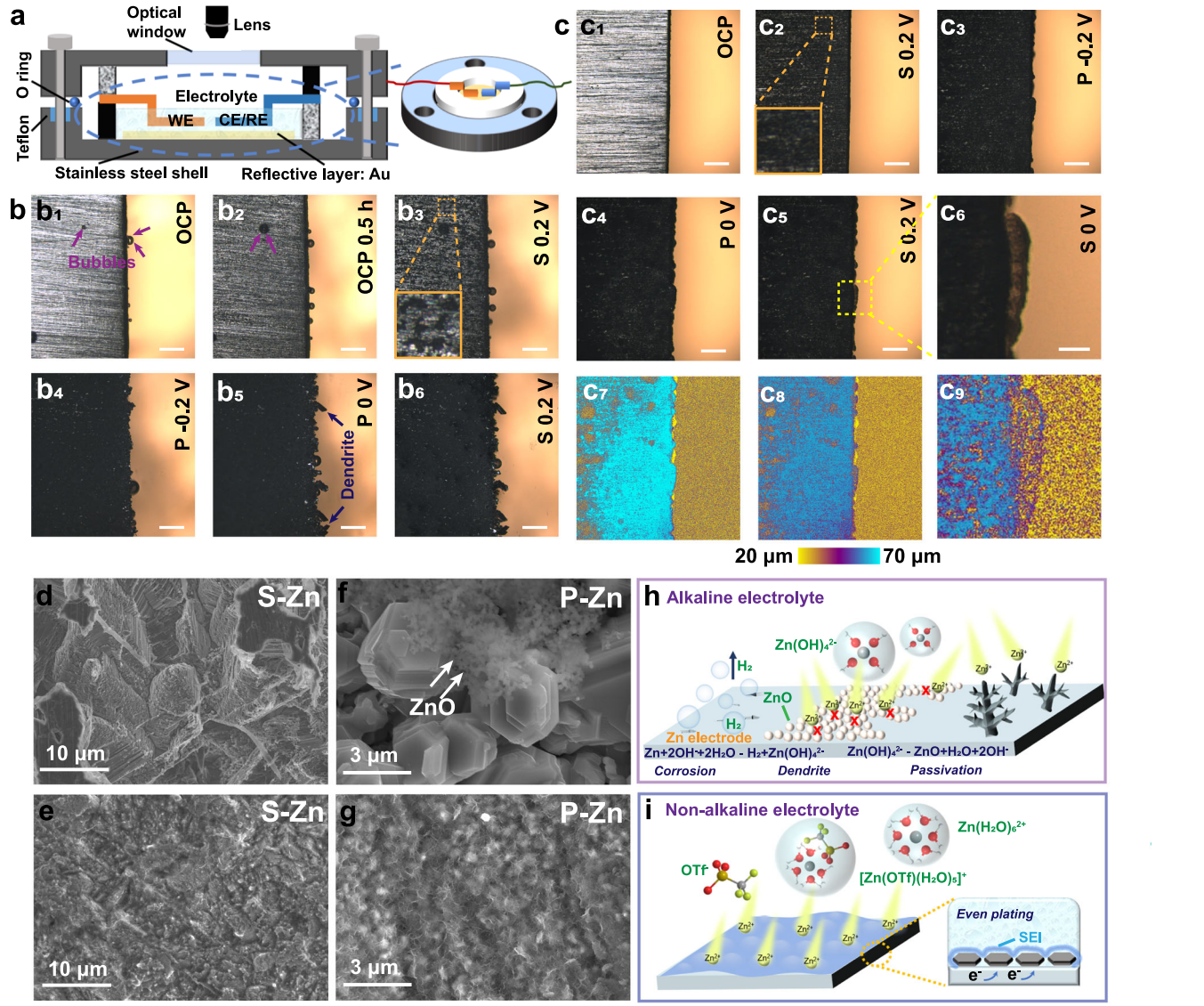

Fig. 4 | In situ OM monitoring of the stripping/plating processes on the Zn electrode during cycling. a Schematic illustration of the in situ electrochemical OM setup. The polished Zn foils were used as the working electrode (WE) and counter electrode (CE)/reference electrode (RE), respectively. **b** In situ OM images of interfacial processes on the Zn electrode at different potentials in 6 M KOH + 0.2 M $Zn(CH_3COO)_2$ electrolyte. **c** In situ (**c_1**–**c_6**) OM and (**c_7**–**c_9**) corresponding height images of interfacial processes on the Zn electrode at different potentials in 1 M $Zn(OTf)_2$ electrolyte. The scale bars are 200 μm in (**b_1**–**c_5**) and 50 μm in (**c_6**). The SEM images of the Zn electrode after the stripping process in (**d**) 6 M KOH + 0.2 M $Zn(CH_3COO)_2$ and (**e**) 1 M $Zn(OTf)_2$ electrolytes, respectively. The SEM images of the Zn electrode after the plating process in (**f**) 6 M KOH + 0.2 M $Zn(CH_3COO)_2$ and (**g**) 1 M $Zn(OTf)_2$ electrolytes, respectively. "S-Zn" means stripped Zn electrode, and "P-Zn" means plated Zn electrode. Schematic illustrations of Zn electrode/electrolyte interfaces in (**h**) 6 M KOH + 0.2 M $Zn(CH_3COO)_2$ and (**i**) 1 M $Zn(OTf)_2$ electrolytes, respectively.

separator. Even after 2nd dissolution process, significant amounts of Zn blocks and dendrites are observed on the Zn surface, indicating poor Zn plating/stripping reversibility (Supplementary Fig. S35a, b). However, a homogeneous film and flat Zn electrode surface are found in the non-alkaline system (Supplementary Fig. S35c, d). This film formed on the Zn electrode may be ascribed to the formation of the solid electrolyte interphase (SEI), which is already present after 1st dissolution (Supplementary Fig. S36a, b) and induces the dendrite-free growth (Fig. 4g and Supplementary Fig. S36c, d). The corresponding schematics of the interfacial processes in alkaline and non-alkaline electrolytes are illustrated in Fig. 4h, i, respectively. It is concluded that the rapid corrosion of the Zn electrode results in the formation of H_2 and $Zn(OH)_4^{2-}$ in alkaline electrolytes. $Zn(OH)_4^{2-}$ easily decomposes into the inert ZnO, which blocks the ion diffusion and aggravates dendrite growth (Fig. 4h). In contrast, the corrosion and passivation issues can be avoided in non-alkaline electrolyte because of the absence of hydroxyl. Uniform SEI forms at the interface, which can induce homogeneous Zn deposition and irreversible dissolution (Fig. 4i).

Interfacial reaction mechanisms in the non-alkaline ZAB

On the basis of the above experimental results, mechanistic insights into the interfacial processes in the non-alkaline ZAB are provided. In 1 M $Zn(OTf)_2$ electrolyte, the hydrophobic OTf^- anion is absorbed on the positive electrode surface to create a water-poor and Zn^{2+}-rich inner Helmholtz plane (IHP) in view of the electrostatic force. In this case, O_2 obtains two electrons from the electrode to generate nanosheet ZnO_2 with a thickness of 1-2 nm (Fig. 5a). It was revealed from the DFT calculations that the two electrons transfer with Zn^{2+} has the lowest free-energy barriers compared with other reactions involving both Zn^{2+} and H_2O[18]. Interestingly, the edges of the nanosheets are surrounded by low-modulus outlines, mainly including C = C and

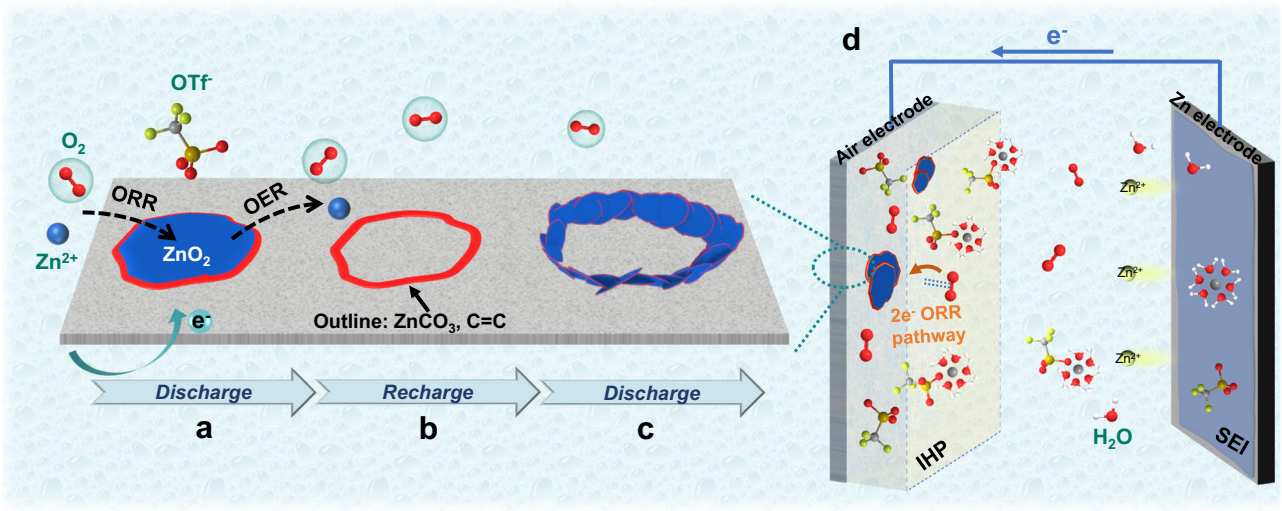

Fig. 5 | Schematic illustration of the interfacial reaction mechanisms in a $Zn(OTf)_2$-based Zn-air cell. The interfacial evolution of the air positive electrode (**a**) upon the 1st discharge showing the horizontal growth of the nanosheet ZnO_2, (**b**) upon the 1st recharge showing the remaining of the surrounding outlines, and (**c**) upon the 2nd discharge showing the nanosheet growth near the outline. **d** Summarization of the overall reaction processes of the ZAB at both positive and negative electrodes.

inorganic $ZnCO_3$ species. Note that the edges exposed in ZnO_2 nanosheets are mainly terminated by oxygen, which possess higher activity due to the more unsaturated dangling bonds[34,35]. Inspired by this, the ions in the electrolyte are adsorbed on the edges[36]. Simultaneously, ZnO_2 nanosheets will transfer electrons to ions, resulting in the reduction of the adsorbed ions to form C = C and $ZnCO_3$[37]. In addition, the width of the outline increases with the number of nanosheet layers. During the recharge process, the nanosheets will be decomposed completely, leaving the low-modulus outlines at the interface. This indicates the excellent reversibility of O_2/ZnO_2 chemistry and stability of the outline structure (Fig. 5b). Remarkably, nanosheet ZnO_2 deposits only near the outlines during the 2nd discharge, which reveals that the ORR activity can be enhanced when such outlines are present on the Pt electrode surface (Fig. 5c). Then, the overall reaction processes of the ZAB in the non-alkaline electrolyte are summarized in Fig. 5d. At the positive electrode side, as discussed above, the O_2 undergoes a two-electron reaction on the Pt electrode and combines with Zn^{2+}, forming ZnO_2 that deposits during the discharge and exhibits satisfactory reversibility during cycling. At the negative electrode side, a homogeneous SEI film can be generated on the electrode surface which induces even dissolution and deposition. The excellent interfacial evolution at both electrode/electrolyte interfaces jointly contributes to the interfacial stability, which in turn, leads to the promising performance of ZABs in non-alkaline electrolyte.

Discussion

In summary, we monitored the real-time Zn-air interfacial evolution in $Zn(OTf)_2$-based non-alkaline electrolyte using in situ AFM and in situ OM in a working battery. The nanosheets ZnO_2 with a thickness of 1-2 nm form at 1.11 V on discharge with the formation of low-modulus materials encircled around it. During the recharge process, the nanosheets are completely decomposed, leaving a circular outline. The outlines consisting of C = C and $ZnCO_3$, are found to improve the ORR performance during the subsequent cycle. Furthermore, the dendrite-free deposition, reversible dissolution processes, and formation of uniform SEI were observed by in situ OM, which is critical for the interfacial stability and reversibility at the Zn electrode. These results provide compelling evidence and an in-depth understanding of the dynamic evolution and reaction pathways at both electrode interfaces, which provide useful information on interfacial constructions and optimized designs for advanced ZABs.

Methods

Preparation of the electrode and electrolyte

Freshly HOPG (ZYH type, Bruker Corp.) was used as the substrate of the working electrode. The Pt nanoparticle electrode was prepared by sputtering Pt on HOPG for 500 s using a Leica EM SCD 500 high vacuum sputter coater. The non-alkaline electrolyte (1 M $Zn(OTf)_2$, pH ≈ 5.3) was prepared by dissolving $Zn(OTf)_2$ (Sigma-Aldrich, 98%) in deionized water according to the molarity. The alkaline electrolyte (6 M KOH + 0.2 M $Zn(CH_3COO)_2$) was prepared by dissolving KOH (Sigma-Aldrich, 99.99%) and $Zn(CH_3COO)_2{\cdot}2H_2O$ (Sigma-Aldrich, 99.999%) in deionized water according to the molarity.

Zn-air coin cell assembly

A polished Zn foil (Alfa Aesar, 99.994%) with a thickness of 0.25 mm and catalyst-loaded carbon cloth (CC, WOS 1002, CeTech) were employed as the negative and positive electrodes, respectively. The electrolyte volume was 150 µL. A cleaned CC substrate was hot-pressed with a gas diffusion layer (GDL, 1.2 × 1.2 cm^2) at 80 °C for 90 s. To fabricate a Pt/C positive electrode, 10 mg Pt/C, and 20.0 µL Nafion solution (5.0 wt%) were first dispersed in a mixture of 990 µL ethanol and 990 µL deionized water, followed by 1 h sonication to form a homogenous catalyst ink. A certain volume of catalyst ink was transferred onto the CC side of the CC/GDL hybrid via a controlled drop casting method to achieve a catalyst loading of 1 mg cm^{-2}.

In situ OM

Polished Zn foils were used as the working and reference/counter electrodes inside a homemade electrochemical cell for in situ OM measurements. The electrolyte volume was about 350 µL. A Teflon plate was positioned in a sealed container with an optical glass window. An "O" ring of per-fluorinated elastomer, with a diameter of 38 mm, was used to seal the cell. In situ OM investigation was carried out by using an optical microscope (OLYMPUS, OLS-4000) with a 10 × objective lens (MPanFLN, numerical aperture value = 0.3) coupled with the electrochemical workstation (ACHI760E, Chenhua, Shanghai) for the experiments. The laser with a wavelength of 405 nm is used as the probing light. For the imaging process, by moving the sample surface

stepwise through the focal plane with a Z-scanning stage, the three-dimensional surface topography can be calculated by assembling of the slices taken at each Z-step. Thus, the height profiles can be obtained. The CV curves were recorded in the range from − 0.2 to 0.2 V at a sweep rate of 0.2 mV s^{-1}. All potentials were referred to Zn^{2+}/Zn.

Electrochemical AFM

In situ AFM monitoring of Zn-O_2 interfacial reactions was realized by assembling a Zn-O_2 model cell onto AFM equipment. In the Zn-O_2 model cell, Pt-modified HOPG served as the working electrode, and Zn strips were employed as the counter and reference electrodes. The electrolyte volume was about 300 µL. The working electrode with an area of 1.2 × 1.2 cm^2 was exposed to the electrolyte that was saturated with O_2 (> 99.999%) for 2 h. A fluorosilicone "O" ring with a diameter of 10 mm was used to seal the cell. In situ electrochemical AFM cell was assembled on the commercial AFM system (Bruker Multimode 8 with Nanoscope V controllers) coupled with an electrochemical workstation. CV curves coupled with AFM scanning were recorded in the range of 0.6-2.1 V at a sweep rate of 1 mV s^{-1}. In situ AFM images were acquired at different potentials. All potentials were referred to Zn^{2+}/Zn. The electrode surface was scanned by a silicon AFM probe (Bruker, k = 1.74 N m^{-1}, f_0 = 90 kHz, rectangular AFM probe tip) with the tip radius of curvature of 10 nm in the mode of PeakForce Quantitative Nano-Mechanics. The scan rates are 0.977 Hz for scan size ≤ 5 µm × 5 µm and 0.62 Hz for 8 µm × 8 µm.

Material characterizations

The electrodes were disassembled from the cells and washed with deionized water to remove the residual electrolyte on the surface. Samples for characterizing the nanosheets and the outlines were obtained after the cell was discharged from OCP to 0.60 V, and subsequently charged to 2.0 V, respectively. SEM (Hitachi S-4800) was employed to image the nanosheets. HRTEM images were obtained by a TEM (IEM 2100 F, IEOL, Japan) with an accelerating voltage of 200 kV. Raman spectroscopy (Thermo Scientific DXRxi) with a laser wavelength of 532 nm and AFM-IR (Bruker) were employed to characterize the chemical composition. XPS analysis was performed on an ESCALab 250Xi (Thermo Fisher) using monochromated Al K_α (1486.6 eV) with an energy of 150 W. The base pressure was about 3×10^{-9} mbar, and the binding energies were referenced to the sp^3 -hybridized carbon C 1 s peak at 284.8 eV. XRD patterns were performed on an Empyrean instrument (PANalytical) in the range from 30° to 42°.

Data availability

All data supporting this study and its findings are available within the article and Supplementary Information. Additional supporting data of this study are available from the corresponding author on request. Source data are provided with this paper.

References

1. Fu, J. et al. Electrically rechargeable Zinc-air batteries: Progress, challenges, and perspectives. *Adv. Mater.* **29**, 1604685 (2017).
2. Liu, J.-N. et al. A brief history of zinc-air batteries: 140 years of epic adventures. *Energy Environ. Sci.* **15**, 4542–4553 (2022).
3. Chen, X. et al. Recent advances in materials and design of electrochemically rechargeable Zinc-air batteries. *Small* **14**, 1801929 (2018).
4. Pan, Z. et al. All-solid-state sponge-like squeezable zinc-air battery. *Energy Storage Mater.* **23**, 375–382 (2019).
5. Jiang, Y. et al. Multidimensional ordered bifunctional air electrode enables flash reactants shuttling for high-energy flexible Zn-air batteries. *Adv. Energy Mater.* **9**, 1900911 (2019).
6. Shang, N. et al. Challenges for large scale applications of rechargeable Zn–air batteries. *J. Mater. Chem. A* **10**, 16369–16389 (2022).
7. Pan, J. et al. Advanced architectures and relatives of air electrodes in Zn–air batteries. *Adv. Sci.* **5**, 1700691 (2018).
8. Liu, X., Zhang, G., Wang, L. & Fu, H. Structural design strategy and active site regulation of high-efficient bifunctional oxygen reaction electrocatalysts for Zn–air battery. *Small* **17**, 2006766 (2021).
9. Zhang, H. et al. A redox-mediated Zinc–air fuel cell. *ACS Energy Lett.* **7**, 2565–2575 (2022).
10. Zhou, Y. et al. Boosting oxygen electrocatalytic activity of Fe–N–C catalysts by Phosphorus incorporation. *J. Am. Chem. Soc.* **145**, 3647–3655 (2023).
11. Han, J. et al. Single-atom Fe-Nx-C as an efficient electrocatalyst for Zinc–air batteries. *Adv. Funct. Mater.* **29**, 1808872 (2019).
12. Wang, Q. et al. Quasi-solid-state Zn-air batteries with an atomically dispersed cobalt electrocatalyst and organohydrogel electrolyte. *Nat. Commun.* **13**, 3689 (2022).
13. Zhao, Y.-X. et al. A "pre-division metal clusters" strategy to mediate efficient dual-active sites ORR catalyst for ultralong rechargeable Zn-air battery. *Angew. Chem. Int. Ed.* **62**, e202216950 (2023).
14. Li, Y. et al. Long-battery-life flexible zinc–air battery with near-neutral polymer electrolyte and nanoporous integrated air electrode. *J. Mater. Chem. A* **7**, 25449–25457 (2019).
15. Li, L. & Manthiram, A. Long-life, high-voltage acidic Zn–air batteries. *Adv. Energy Mater.* **6**, 1502054 (2016).
16. Chen, H. et al., High-performance neutral Zinc-air batteries based on hybrid Zinc/Carbon nanotube fiber anodes. *Adv. Mater. Technol.* **8**, 2301217 (2023).
17. Leong, K. W. et al. Rechargeable Zn-air batteries: Recent trends and future perspectives. *Renew. Sustain. Energy Rev.* **154**, 111771 (2022).
18. Sun, W. et al. A rechargeable Zinc-air battery based on Zinc peroxide chemistry. *Science* **371**, 46–51 (2021).
19. Hou, Y. et al. MBene promoted Zn peroxide chemistry in rechargeable near-neutral Zn–air batteries. *Energy Environ. Sci.* **16**, 3407–3415 (2023).
20. Sun, W., Küpers, V., Wang, F., Bieker, P. & Winter, M. A non-alkaline electrolyte for electrically rechargeable Zinc-air batteries with long-term operation stability in ambient air. *Angew. Chem. Int. Ed.* **61**, e202207353 (2022).
21. Jin, S. et al. Production of fast-charge Zn-based aqueous batteries via interfacial adsorption of ion-oligomer complexes. *Nat. Commun.* **13**, 2283 (2022).
22. Yang, Q. et al. Dendrites in Zn-based batteries. *Adv. Mater.* **32**, 2001854 (2020).
23. He, Y. et al. In-situ observation of the gas evolution process on the air electrode of Zn-air batteries during charging. *Chem. Eng. J.* **427**, 130862 (2022).
24. Shen, Z.-Z. et al. Revealing the CO_2 conversion at electrode/electrolyte interfaces in Li–CO_2 batteries via nanoscale visualization methods. *Angew. Chem. Int. Ed.* **63**, e202316781 (2024).
25. He, Y., Cui, Y., Shang, W., Zhao, Z. & Tan, P. Insight into the bubble-induced overpotential towards high-rate charging of Zn-air batteries. *Chem. Eng. J.* **448**, 137782 (2022).
26. Lang, S., Yu, S.-H., Feng, X., Krumov, M. R. & Abruña, H. D. Understanding the lithium–sulfur battery redox reactions via operando confocal Raman microscopy. *Nat. Commun.* **13**, 4811 (2022).
27. Xu, B. et al. Gel adsorbed redox mediators tempo as integrated solid-state cathode for ultra-long life quasi-solid-state Na–air battery. *Adv. Energy Mater.* **13**, 2302325 (2023).
28. Hu, X.-C. et al. Insight into interfacial processes and degradation mechanism in magnesium metal batteries. *Nano Energy* **78**, 105338 (2020).
29. Verma, S. & Jain, S. L. Nanosized zinc peroxide (ZnO_2): a novel inorganic oxidant for the oxidation of aromatic alcohols to carbonyl compounds. *Inorg. Chem. Front.* **1**, 534–539 (2014).
30. Escobedo-Morales, A. et al. Structural and vibrational properties of hydrothermally grown ZnO_2 nanoparticles. *J. Cryst. Growth* **316**, 37–41 (2011).

31. Larroumet, D., Greenfield, D., Akid, R. & Yarwood, J. Spectroscopic studies of the corrosion of model iron electrodes in carbonate and phosphate buffer solutions. *J. Raman Spectrosc.* **39**, 1740–1748 (2008).
32. Drmosh, Q. A., Gondal, M. A., Yamani, Z. H. & Saleh, T. A. Spectroscopic characterization approach to study surfactants effect on ZnO_2 nanoparticles synthesis by laser ablation process. *Appl. Surf. Sci.* **256**, 4661–4666 (2010).
33. Hussein, H. M., Ghafoor, D. D. & Omer, K. M. Room temperature and surfactant free synthesis of zinc peroxide (ZnO_2) nanoparticles in methanol with highly efficient antimicrobials. *Arab. J. Chem.* **14**, 103090 (2021).
34. Tang, K., Wang, X., Li, Q. & Yan, C. High edge selectivity of in situ electrochemical Pt deposition on edge-rich layered WS_2 nanosheets. *Adv. Mater.* **30**, 1704779 (2018).
35. Liu, S. et al. Facile preparation of novel and active 2D nanosheets from non-layered and traditionally non-exfoliable earth-abundant materials. *J. Mater. Chem. A* **7**, 15411–15419 (2019).
36. Jaramillo, T. F. et al. Identification of active edge sites for electrochemical H_2 evolution from MoS_2 nanocatalysts. *Science* **317**, 100–102 (2007).
37. Kibsgaard, J., Chen, Z., Reinecke, B. N. & Jaramillo, T. F. Engineering the surface structure of MoS_2 to preferentially expose active edge sites for electrocatalysis. *Nat. Mater.* **11**, 963–969 (2012).

Acknowledgements

This work was financially supported by the CAS Project for Young Scientists in Basic Research (Grant No. YSBR-058 to R.W.), the National Key R&D Program of China (Grant No. 2021YFB2500300 to R.W.), the National Natural Science Foundation of China (Grant No. 92372125 to R.W., Grant No. 22205241 to Z.-Z.S.) and the National Postdoctoral Program for Innovative Talents (Grant No. BX20220306 to Z.-Z.S.) of the Chinese Postdoctoral Science Foundation. The authors would like to thank Dr. Shu-Meng Chi of the Experimental Center of Advanced Materials, Beijing Institute of Technology for the AFM-IR and nanoIR characterizations.

Author contributions

R.W. proposed the concepts. J.W. designed and carried out the experiments. Y.L.Z. conducted the Raman studies. J.W., S.-Y.L., Z.-Z.S., G.-X.L., Y.-X.S., R.-Z.L., and B.L. analyzed the data. R.W. supervised the research. J.W. and R.W. wrote the paper. All authors discussed the results and commented on the manuscript.

Competing interests

The authors declare no competing interests.

Additional information

Supplementary information The online version contains supplementary material available at https://doi.org/10.1038/s41467-024-55239-1.

Correspondence and requests for materials should be addressed to Rui Wen.

Peer review information *Nature Communications* thanks Fujun Li, and the other anonymous reviewers for their contribution to the peer review of this work. A peer review file is available.